J. Fluid Mech. (2010), *vol.* 646, *pp.* 297–325. © Cambridge University Press 2010
doi:10.1017/S0022112009993284

Transition to turbulence in the boundary layer over a smooth and rough swept plate exposed to free-stream turbulence

LARS-UVE SCHRADER, SUBIR AMIN AND LUCA BRANDT†

Linné Flow Centre, KTH Mechanics, SE-100 44 Stockholm, Sweden

(Received 20 December 2008; revised 3 November 2009; accepted 4 November 2009)

Receptivity, disturbance growth and transition to turbulence of the three-dimensional boundary layer developing on a swept flat plate are studied by means of numerical simulations. The flow is subject to a favourable pressure gradient and represents a model for swept-wing flow downstream of the leading edge and upstream of the pressure minimum of the wing. The boundary layer is perturbed by free-stream turbulence and localized surface roughness with random distribution in the spanwise direction. The intensity of the turbulent free-stream fluctuations ranges from conditions typical for free flight to higher levels usually encountered in turbomachinery applications. The free-stream turbulence initially excites non-modal streak-like disturbances as in two-dimensional boundary layers, soon evolving into modal instabilities in the form of unsteady crossflow modes. The crossflow modes grow faster than the streaks and dominate the downstream disturbance environment in the layer. The results show that the receptivity mechanism is linear for the disturbance amplitudes under consideration, while the subsequent growth of the primary disturbances rapidly becomes affected by nonlinear saturation in particular for free-stream fluctuations with high intensity. Transition to turbulence occurs in the form of localized turbulent spots randomly appearing in the flow. The main features of the breakdown are presented for the case of travelling crossflow vortices induced by free-stream turbulence. The flow is also receptive to localized roughness strips, exciting stationary crossflow modes. The mode with most efficient receptivity dominates the downstream disturbance environment. When both free-stream fluctuations and wall roughness act on the boundary layer at the same time, transition is dominated by steady crossflow waves unless the incoming turbulence intensity is larger than about 0.5 % for roughness amplitudes of about one tenth of the boundary-layer displacement thickness. The results show that a correct prediction of the disturbance behaviour can be obtained considering the receptivity and evolution of individual modes. In addition, we provide an estimate for the amplitudes of the external disturbance sources above which a fully nonlinear receptivity analysis is necessary.

1. Introduction

Receptivity, disturbance growth and breakdown are the fundamental stages through which laminar flow becomes turbulent. Numerous issues are involved in the transition

† Email address for correspondence: luca@mech.kth.se

process, for example how external perturbations enter the boundary layer and excite internal disturbances (receptivity), how the latter grow (instability), and when and where the flow first becomes turbulent (breakdown). The relevance of these issues is closely related to applications, where, for instance, drag reduction on aircraft wings by suppression or downstream delay of transition is of interest (flow control).

1.1. *Transition in two-dimensional boundary layers*

The classical transition scenario in two-dimensional boundary layers originates from exponentially growing Tollmien–Schlichting (T-S) waves and is observed in flows with low background disturbance levels. When these primary waves grow above a threshold amplitude, the flow becomes susceptible to secondary instability that is three-dimensional in nature and characterized by the occurrence of lambda-shaped vortices (cf. the reviews by Herbert 1988 and Kachanov 1994). Several experiments (see e.g. Taylor 1939; Klebanoff 1971; Westin *et al.* 1994) reveal, however, that transition in boundary-layer flows exposed to free-stream turbulence with intensity $\gtrsim 1\,\%$ of the free-stream velocity is initiated by the growth of perturbations elongated in the streamwise direction rather than by T-S waves. These take the form of streaks with high and low streamwise velocity alternating in the spanwise direction. The streamwise velocity perturbations of the streaks are due to the wall-normal displacement of fluid particles in shear flows by weak pairs of counter-rotating streamwise vortices (lift-up mechanism). The lift-up is promoted by low-frequency oscillations of the turbulent free stream, whereas the high-frequency components are highly damped inside the shear layer (Jacobs & Durbin 1998; Zaki & Saha 2009). As the streaks grow downstream, they become susceptive to high-frequency secondary instability triggered by free-stream turbulence (Zaki & Durbin 2005; Hœpffner & Brandt 2008) or by streak interactions (Brandt & de Lange 2008), and breakdown to turbulent spots is initiated. These spots appear at random locations, grow in size and number and merge with each other until the flow is fully turbulent (bypass transition). A detailed numerical analysis of bypass transition under free-stream turbulence can be found in Jacobs & Durbin (2001) and Brandt, Schlatter & Henningson (2004).

1.2. *Transition in three-dimensional boundary layers*

Boundary layers on swept wings, plates and wedges, on cones or on rotating disks are three-dimensional, and the transition mechanisms differ from those in two-dimensional flow owing to the existence of different instability types. Saric, Reed & White (2003) list four kinds of instabilities, relevant in different regions of the boundary layer: attachment-line, Görtler, streamwise (T-S waves) and crossflow instabilities. The focus is here on the crossflow instability type in accelerated swept-plate flow. Crossflow instability is related to the inflectional velocity profile of the cross component of the mean flow. The base flow is therefore susceptive to strong inviscid instability, which can be both steady and unsteady (see also the review article by Bippes 1999). Crossflow disturbances are intensified in the forward part of a wing by the favourable pressure gradient, whereas growth of T-S waves is suppressed in this region. These become instead relevant in the decelerating flow in the rear portion of the wing.

Whether steady or unsteady crossflow waves lead to transition of swept flow is a relevant issue for the correlation between wind-tunnel experiments and free-flight tests with significantly lower levels of external vortical disturbances. Experiments by

Deyhle & Bippes (1996) and White *et al.* (2001) and numerical studies by e.g. Crouch (1993), Choudhari (1994) and Schrader, Brandt & Henningson (2009) suggest that steady crossflow modes induced by wall roughness dominate in an environment of low-amplitude free-stream disturbances (at free-flight conditions), whereas travelling modes become dominant at higher intensities of the background disturbance (in turbomachines or some wind-tunnel tests). As the crossflow waves grow downstream in amplitude, they distort the chordwise mean-velocity profiles in the spanwise direction such that the flow becomes susceptive to high-frequency secondary instability. Results of the secondary instability of swept-wing flow based on the parabolized stability equations (PSE) are available in Malik *et al.* (1999) and Haynes & Reed (2000); findings from direct numerical simulation (DNS) are presented by Wintergerste & Kleiser (1997) for the temporal framework and by Högberg & Henningson (1998) and Wassermann & Kloker (2002, 2003) for spatially evolving flows. Flow control in swept-wing boundary layers has been addressed experimentally by Saric, Carillo & Reibert (1998). These authors used arrays of distributed roughness elements with different spanwise spacing near the leading edge of a swept wing. They show that the most amplifying steady crossflow mode can be suppressed if the spacing between the roughness elements is smaller than the most unstable spanwise wavelength. Under these conditions, a less unstable, 'useful' crossflow mode becomes dominant, and transition to turbulence occurs farther downstream than in the uncontrolled scenario. Wassermann & Kloker (2002) confirmed this passive control strategy by means of DNS.

This work studies receptivity, growth and breakdown of crossflow instability in swept-plate flow under free-stream turbulence, surface roughness and the combination of both by means of nonlinear large-eddy simulation (LES) and DNS. This type of simulations is presented here for the first time. In a previous investigation, Schrader *et al.* (2009) analysed linear receptivity mechanisms in swept boundary layers. These authors isolated the effect of different components of free-stream disturbances, modelled by single free-stream Orr–Sommerfeld modes, and demonstrated that travelling crossflow modes can be forced by vortical disturbances in the free stream via a scale-conversion process. In addition, scattering of free-stream modes on chordwise localized surface roughness with spanwise periodicity was examined and shown to become relevant only for high levels of free-stream turbulence.

However, in three-dimensional boundary layers, the interaction between exponentially growing modes may continuously induce waves with large amplification and quickly create a disturbed boundary-layer flow. To better analyse this scenario, full nonlinear simulations are needed and presented here. We employ a more complex model for free-stream vorticity by considering the superposition of a large number of Orr–Sommerfeld/Squire modes with a turbulent energy spectrum. Localized roughness with spanwise random amplitude is modelled through a sum of Fourier modes. These disturbance sources will bring nonlinear effects into play and provide a more complete picture of receptivity and transition in three-dimensional boundary layers. Moreover, we investigate herein the breakdown of the three-dimensional boundary layer. The first part of the results is meant to illustrate the disturbance features inside the shear layer during growth, saturation and breakdown of the primary instabilities induced by free-stream turbulence. In the second part, the focus is on the early receptivity process, where receptivity of unsteady and steady crossflow instability is compared with the linear results of Schrader *et al.* (2009).

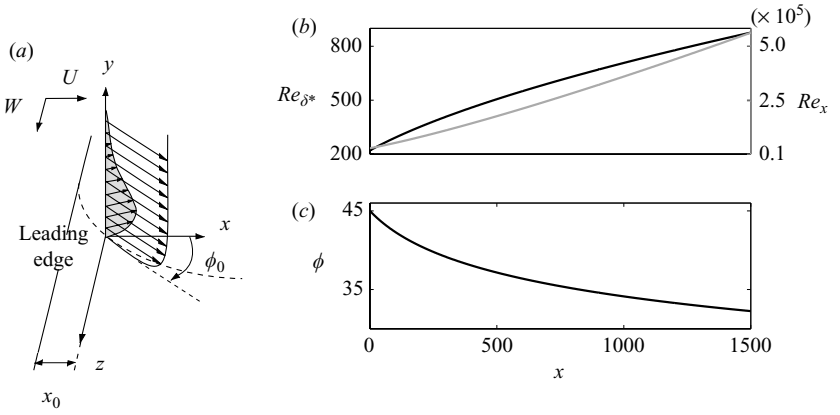

FIGURE 1. (*a*) Wall-normal profiles of streamwise and crossflow velocities for Falkner–Skan–Cooke boundary-layer flow. (*b*) Reynolds number based on displacement thickness (black) and downstream location (grey) versus chord coordinate. (*c*) Angle of external streamline along chordwise coordinate.

2. Flow configuration and numerical approach

2.1. *Base flow*

Here, boundary-layer flow over a swept flat plate is considered. The mean flow is obtained by solving the Navier–Stokes equations with Falkner–Skan–Cooke velocity profiles as the initial condition. This configuration often serves as a prototype for swept-wing boundary-layer flow, including many of its characteristics such as chordwise pressure gradient, streamline curvature and crossflow, while leading edge and surface curvature are not taken into account. The stream- and cross-wise velocity profiles of swept-plate flow are depicted in figure 1(*a*), where the coordinate system adopted is also shown. The basic flow is completely described by the Reynolds number, the Hartree parameter and the sweep angle. These are chosen in correspondence with the values in Schrader *et al.* (2009). This set of parameters defines conditions similar to those of the airfoil experiments at Arizona State University reported by Reibert *et al.* (1996). The chordwise pressure gradient is quantified by the Hartree parameter β_H, chosen to be $\beta_H = 0.333$. This establishes a favourable pressure-gradient boundary layer with chordwise flow acceleration:

$$U^*_\infty(x^*) = U^*_{\infty,0}\left(\frac{x^* + x^*_0}{x^*_0}\right)^{\beta_H/(2-\beta_H)} \quad \text{and} \quad W^*_\infty = U^*_{\infty,0}\tan\phi_0, \tag{2.1}$$

where U and W indicate chord- and spanwise mean velocity and the asterisk denotes dimensional quantities. The sweep angle $\phi_0 = 45^\circ$ is defined at a reference station x^*_0, which corresponds to the inflow plane of the computational domain. The sweep together with chordwise flow acceleration causes curved streamlines and a force imbalance inside the boundary layer, driving a secondary mean-flow component in the cross-stream direction, the crossflow. The sweep angle under investigation is characterized by significant crossflow and thus by strong crossflow instability.

Lengths are normalized by the chordwise boundary-layer displacement thickness $\delta^*_0 \equiv \delta^*(x_0)$ at the reference location x_0 and velocities by the chordwise free-stream velocity $U_{\infty,0} \equiv U_\infty(x_0)$. Reference length and velocity define the Reynolds number at

the computational inlet,

$$Re_{\delta_0^*} = \frac{U_{\infty,0}\delta_0^*}{\nu}, \tag{2.2}$$

where ν is the kinematic viscosity. The local Reynolds number Re_{δ^*} is obtained by replacing δ_0^* and $U_{\infty,0}$ in (2.2) by their local values. The inflow Reynolds number is fixed at $Re_{\delta_0^*} = 220$. The Reynolds number Re_x based on the chordwise location is also common in literature, related to $Re_{\delta_0^*}$ via

$$Re_x = [x_0 U_{\infty,0} + x U_\infty(x)] Re_{\delta_0^*}. \tag{2.3}$$

Figure 1(*b*) shows the Reynolds numbers Re_{δ^*} and Re_x and figure 1(*c*) shows the local angle ϕ of the external streamline versus the chordwise coordinate x for the configuration adopted here.

2.2. *Numerical method*

The present results are obtained using a spectral method to solve the three-dimensional time-dependent incompressible Navier–Stokes equations; see Chevalier *et al.* (2007). The simulation code builds on a Fourier representation along the chord- and spanwise coordinates x and z and on Chebyshev polynomials in the wall-normal direction y, along with a pseudo-spectral treatment of the nonlinear terms. A zero-slip condition is imposed along the wall for the base flow and the perturbed flow (base flow plus disturbances). For the simulations with free-stream turbulence, von Neumann conditions are applied in Fourier space at the far-field boundary above the plate. To reduce the computational effort, the top boundary for the simulations with surface roughness has been placed nearer the plate, achieved by using the asymptotic conditions first proposed by Malik, Zang & Hussaini (1985). Periodic boundary conditions are enforced in the spanwise and chordwise directions z and x. The swept-plate flow develops along x: the boundary layer grows and the streamlines change direction continuously. Nonetheless, to obtain the chordwise periodicity required by a Fourier representation, a 'fringe region' is used at the downstream end of the computational domain, as described by Nordström, Nordin & Henningson (1999). In this region, the velocity field is forced to the desired inflow velocity profiles; they consist of the Falkner–Skan–Cooke similarity profiles in the present case with/without incoming free-stream disturbances.

To validate the present implementation, we show in figure 2 the chordwise evolution of a steady crossflow mode as obtained with two different spectral methods. The mode is computed for $Re_{\delta_0^*} = 220$, inserted in the fringe region of the present spectral code and prescribed as an inflow condition of a simulation using a spectral element method. The spectral element code (see Tufo & Fischer 1999) builds on an inflow–outflow formulation rather than a fringe technique. Good agreement of the modal N factor and the growth rate σ is obtained for the two spectral methods. As we will later show results from PSE calculations we also validate the PSE code in figure 2: the PSE results compare well with the numerical solutions of the Navier–Stokes equations (see also Tempelmann, Hanifi & Henningson 2009).

2.3. *Subgrid-scale modelling*

This study requires a computational domain of rather large spanwise and wall-normal size to accommodate a free-stream turbulence field with a wide enough range of length scales. The resolution of all scales would, however, result in prohibitively large computational costs such that the simulations are only affordable by employing an LES model. The ADM-RT subgrid-scale (SGS) model by Schlatter, Stolz & Kleiser

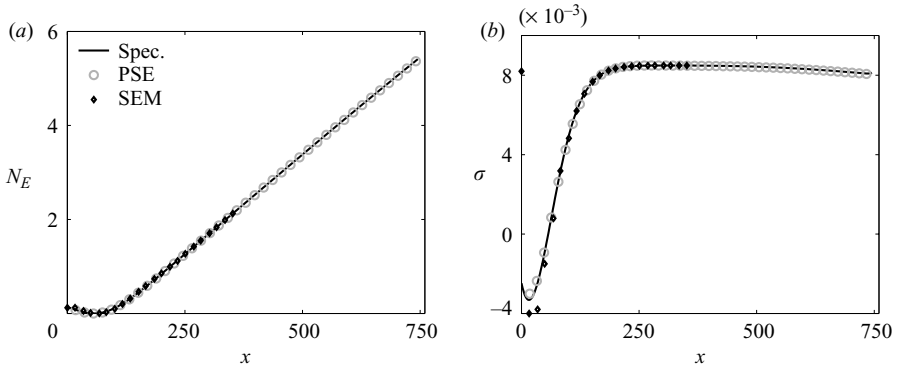

FIGURE 2. (*a*) *N*-factor for energy and (*b*) growth rate of the steady crossflow mode with spanwise wavenumber $\beta = -0.19$, initialized at $Re_{\delta_0^*} = 220$. Comparison between results from the present spectral code (black), a spectral element method (SEM; black diamonds) and a PSE calculation (grey circles).

(2004) is used for the present simulations, building on the approximate deconvolution model (ADM). This model has been successfully applied in incompressible transitional and turbulent flow (see e.g. the recent work by Monokrousos *et al.* 2008). The main ingredient of the ADM-RT model is the so-called relaxation term (RT) used as a closure for the subgrid-scale stresses τ_{ij},

$$\frac{\partial \tau_{ij}}{\partial x_j} = \chi H_N * \bar{u}_i \quad \text{with} \quad H_N = (I - G)^{N+1}. \tag{2.4}$$

Here, $\bar{u}_i$ indicates the velocity field implicitly filtered by the reduced resolution of the LES grid, and H_N denotes a three-dimensional high-pass filter of high order derived from the low-order low-pass filter G of Stolz, Adams & Kleiser (2001), and the star stands for convolution in physical space. Here, H_N is characterized by the exponent $N = 5$ and the cutoff wavenumber $\kappa_c = 2\pi/3$ of the filter G. Numerical stability is ensured by a model coefficient χ in the range $0 \leqslant \chi \leqslant 1/\Delta t$. Here, we chose $\chi = 0.2$, as in Schlatter, Stolz & Kleiser (2006), Schlatter, de Lange & Brandt (2007) and Monokrousos *et al.* (2008). The role of the RT term in (2.4) is to drain kinetic energy from the resolved fluctuations at the smallest represented length scale and thereby to model the impact of the unresolved motion on the resolved structures. Note that all simulations were performed adding the subgrid-scale stresses. However, the computations focusing on the boundary-layer receptivity consider only the initial phase of the disturbance growth. In these cases, the extra relaxation term is practically zero and the computations can be considered as DNS.

2.4. *Disturbance generation*

Two different disturbance sources are considered: a vortical perturbation in the free stream and a roughness element on the wall near the inflow plane of the computational domain. These two types of disturbances are listed in the review article by Saric *et al.* (2003) as particularly relevant in swept boundary layers. The free-stream turbulence at the inflow plane and the roughness element are shown in figures 3(*a*) and 3(*b*), and their numerical generation is described below.

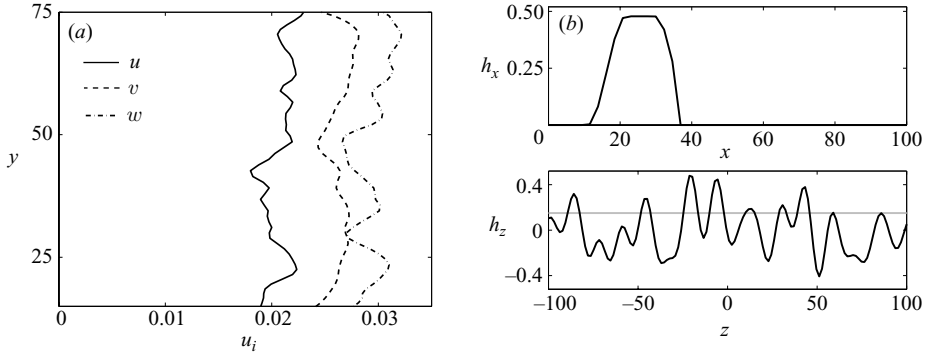

FIGURE 3. (*a*) Turbulent free-stream fluctuations at the inflow plane of the computational domain for a turbulence intensity of 2.53 % of $U_{\infty,0}$. (*b*) Chord- and spanwise contours of the wall roughness. The r.m.s. amplitude is 0.15 (dashed line).

2.4.1. *Free-stream turbulence*

The turbulent inflow disturbances are numerically generated as in Jacobs & Durbin (2001) and Brandt *et al.* (2004), i.e. by the superposition of eigenmodes from the continuous spectrum of the Orr–Sommerfeld and Squire operator—however, modified here for the Falkner–Skan–Cooke base flow. A wave vector is associated with each free-stream mode, where the complex chordwise wavenumber α is the eigenvalue of the corresponding Orr–Sommerfeld and Squire problem and the wall-normal wavenumber γ determines the position along the continuous spectrum (see e.g. Schmid & Henningson 2001). After choosing the spanwise and wall-normal wavenumbers β and γ and angular frequency ω, the eigenvalue α of the continuous-spectrum modes can be obtained from analytical expressions (see Schrader *et al.* 2009, for swept boundary layers). The velocity profiles pertaining to each eigenfunction are computed numerically, whereas the free-stream behaviour can also be obtained analytically.

An isotropic perturbation field is obtained in Fourier space by considering 20 concentric spherical shells of radius κ spanning the range of wave vectors of length $\kappa_l \leqslant \kappa \leqslant \kappa_u$. The limits κ_l and κ_u depend on the size and resolution of the computational domain and are chosen to be $\kappa_l = 0.05$ and $\kappa_u = 1.1$. The frequency range covered by the turbulence model is $1.5 \times 10^{-4} \leqslant |\omega| \leqslant 1.1$. Forty points are distributed with constant spacing on each shell: these define the wave vectors and continuous-spectrum eigenmodes to be included in the expansion for the free-stream disturbance,

$$\boldsymbol{u}_{FST} = \sum_{k=1}^{20} a_k \sum_{l=1}^{40} \hat{\boldsymbol{u}}_{kl}(y;\gamma) \mathrm{e}^{\mathrm{i}(\alpha_{kl}x + \beta_{kl}z - \omega_{kl}t)}, \tag{2.5}$$

where $\hat{\boldsymbol{u}}_{kl}$ denotes the wall-normal disturbance–velocity profiles of the free-stream mode and contains the wall-normal oscillations. The randomness inherent in turbulent fields is obtained through a random rotation of the shells, provided by random phase angles of the complex coefficients a_k in (2.5) as well as by the random phase in the complex function $\hat{\boldsymbol{u}}_{kl}$. The energy density pertaining to the wavenumber κ_k of the kth shell is equally distributed among all modes on the shell, and the energy distribution across the wavenumbers included is approximated by the von Kármán spectrum. Details of the spectrum can be found in Brandt *et al.* (2004). The relevant measure for the disturbance amplitude is the turbulence intensity Tu,

ε_h	h_{start}	h_{end}	h_{rise}	h_{fall}
0.0375, 0.075, 0.15	6	34	12	12

TABLE 1. Parameters of the surface-roughness shape.

defined as $Tu = \sqrt{(1/3)(\overline{u^2} + \overline{v^2} + \overline{w^2})}$. The wall-normal distribution of the free-stream fluctuations at the inlet is depicted in figure 3(*a*).

We conclude by noting that the quantitative results on the boundary-layer response will depend on the turbulence model spectrum chosen; the relevant physics, on the other hand, will be independent of the spectrum if the receptivity process is linear and if there is no significant nonlinear interaction in the free stream. In that case, the amplitude of the boundary-layer disturbances will be proportional to the amplitude of the free-stream modes, with the turbulence intensity Tu_0 being the factor of proportionality. We will show below that this holds for most of the Tu_0 values studied. The random phases used for the combination of the continuous modes do not correctly reproduce the energy transfer in a natural turbulent flow. However, these effects appear to be relevant only for the largest Tu_0 examined, as shown below; moreover, the synthetic inflow will adjust to the mean-flow conditions farther downstream.

2.4.2. *Surface roughness*

The surface roughness is modelled through non-homogeneous boundary conditions for the disturbance velocities u and w at the wall,

$$\begin{pmatrix} u \\ v \\ w \end{pmatrix}_{wall} = \begin{cases} \begin{pmatrix} -h(x,z)\dfrac{\partial U}{\partial y} \\ 0 \\ -h(x,z)\dfrac{\partial W}{\partial y} \end{pmatrix}_{wall}, & h_{start} \leqslant x \leqslant h_{end} \\ \mathbf{0}, & \text{elsewhere.} \end{cases} \tag{2.6}$$

In the expression above, $h(x, z)$ is the shape of the roughness bump

$$h(x, z) = \varepsilon_h h_x(x) h_z(z), \tag{2.7}$$

with the amplitude ε_h and the functions $h_x(x)$ and $h_z(z)$ along the chord- and spanwise coordinates, respectively. The function $h_x(x)$ builds on a smooth, localized step function (cf. Schrader *et al.* 2009), rising from $x = h_{start}$ along the flank h_{rise}, falling till $x = h_{end}$ along h_{fall} and centred at the location $x_r = (h_{start} + h_{end})/2$, the nominal roughness station (see figure 2*b* and table 1). This particular shape is characterized by a broad spectrum of chordwise wavenumbers, giving rise to a broadband disturbance including unstable modes. The function $h_z(z)$ is obtained through an expansion in sinusoidal functions with 16 different spanwise wavenumbers and random phases,

$$h_z(z) = \sum_{n=1}^{16} \sin\left(n\beta_0 z + \phi_n^{rand}\right), \tag{2.8}$$

where the fundamental spanwise wavenumber $\beta_0 = 2\pi/L_z$ is defined by the spanwise width L_z of the computational domain and ϕ_n^{rand} are random angles. The characteristic

Box	$Re_{\delta^*,0}$	$L_x \times L_y \times L_z$	$N_x \times N_y \times N_z$	L_{fringe}
L	220	$1500 \times 90 \times 200$	$768 \times 121 \times 128$	135
S	220	$750 \times 90 \times 200$	$384 \times 121 \times 128$	80

TABLE 2. Size and resolution of the computational domains 'L' and 'S', length of the fringe region and inflow Reynolds number.

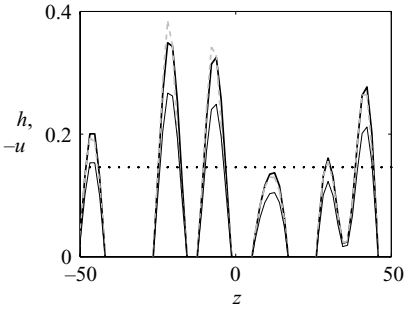

FIGURE 4. Validation of the roughness model for the highest roughness ($\varepsilon_h = 0.15$, dotted line). Comparison between the specified shape $h(x_r, z)$ at the roughness station x_r (—) with the no-slip contour $u = 0$ (grey ----). $-u(x_r, y = 0)$ is plotted as well for comparison (—— thin).

roughness height ε_h in (2.7) is

$$\varepsilon_h = \sqrt{\overline{h_z^2}}\Big|_{x_r}, \tag{2.9}$$

i.e. the root mean square (r.m.s.) of the random spanwise hump contour at the roughness station x_r. Figure 4 gives a validation of the roughness model for the highest roughness ($\varepsilon_h = 0.15$): good agreement is found when comparing the prescribed shape $h(x_r, z)$ at the roughness station x_r with the no-slip contour $u = 0$.

The present roughness model is linear in ε_h; this assumption is valid only for small enough roughness elements. Figure 8 of Schrader *et al.* (2009) gives the range of ε_h for which roughness receptivity is linear in ε_h. The present roughness elements—similar to shape I in that reference—are in the linear range of that figure. Moreover, the individual amplitudes of the 16 modes included in (2.8) are smaller than ε_h; the present bumps can therefore be considered as low-amplitude roughness. The use of a linear roughness model is hence justified for the values of ε_h considered.

2.5. *Computational domain*

Two computational domains with different chordwise length are used: a long one, 'L', to capture the breakdown of the boundary layer and a short one labelled 'S' for the receptivity study. The size $L_x \times L_y \times L_z$, resolution $N_x \times N_y \times N_z$ and length L_{fringe} of the fringe region of the boxes L and S are listed in table 2 together with the Reynolds number $Re_{\delta^*,0}$ defining the location of the inflow plane.

2.5.1. *Domain size and resolution study*

The resolution in wall-normal direction y is finer than that in the wall-parallel planes (see table 2), in particular inside the boundary layer due to the clustering of the Chebyshev points near the wall. The normal resolution is in fact comparable with that of Brandt *et al.* (2004), where no SGS model was used. Since the flow is

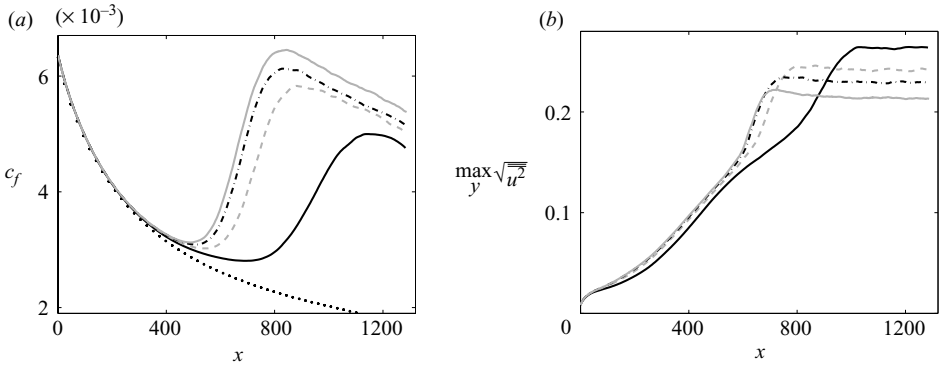

FIGURE 5. Boundary-layer response to free-stream turbulence with $Tu_0 = 3.73\,\%$ and $L = 10$. Study of the influence of chordwise resolution Δx of the computational domain on (*a*) the skin-friction coefficient (dots: Falkner–Skan–Cooke solution) and (*b*) the evolution of the wall-normal maximum of u_{rms}. $\Delta x = 5.86$ ($N_x = 256$) (—); 3.91 ($N_x = 384$) (grey ----); 2.93 ($N_x = 512$) (-·-·-) and 1.95 ($N_x = 768$) (grey ——).

swept at 45°, the resolution requirements in the x and z directions are expected to be similar. The laminar structures preceding the breakdown—the crossflow modes—can thus be fully resolved, while the SGS model will compensate mainly for unresolved small wall-parallel scales occurring at and after the turbulent breakdown. Owing to a wall-normal resolution typical for DNS, the resolution study is restricted to the chord- and spanwise directions. Figure 5 shows the influence of the chordwise resolution in (*a*) on the skin-friction coefficient and in figure 5(*b*) on the chordwise fluctuation amplitude in terms of the maximum of the r.m.s. The transition location, identified by the rapid increase of the skin friction, moves drastically upstream as the chordwise resolution is refined from $\Delta x = 5.86$ to 3.91. This trend becomes slower at a further increase in resolution, and the transition location is observed at nearly the same downstream location when the numerical resolution is further refined from $\Delta x = 2.93$ to 1.95. Figure 5(*b*) shows that, while the early transient and linear growth phase is captured with similar accuracy in the different cases, the subsequent rapid amplification observed around $x \approx 600$ is underpredicted on the coarser domains. Small structures responsible for the excitation of the secondary instability need to be represented on the grid for the correct prediction of the transition location. This requirement is met on the fine meshes, and a further refinement below $\Delta x = 1.95$ will only weakly affect the results while significantly increasing the computational costs. The differences in the maximum levels of c_f and u_{rms} observed in the regime after transition are due to the different range of resolved scales, and uncertainties in the turbulent fluctuations associated with resolution may therefore be relevant for $x \gtrsim 700$ when $Tu_0 = 3.73\,\%$. However, we do not investigate the turbulent regime here; the main focus of the paper is on the receptivity phase and the structures at the breakdown stage. The SGS model is not designed to effect the physics of transition but to prevent unphysical parasitic upstream influences from the highly fluctuating turbulent region farther downstream for simulations where transition occurs (see also Schlatter *et al.* 2006).

On the short domain S, on the other hand, a finer resolution is computationally feasible. Two modifications of box S in table 2 are considered, first a refinement in the streamwise direction, from $\Delta x = 1.95$ to 1.46, and second a higher resolution (1.5 times) in the z direction. The vortical perturbation prescribed at the inlet of

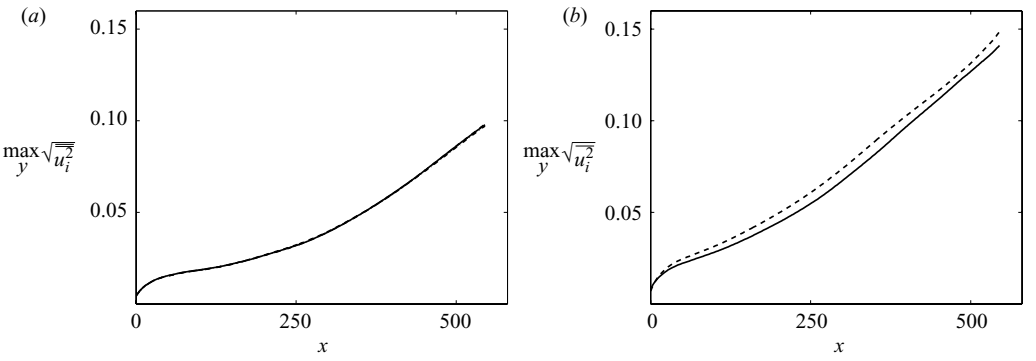

FIGURE 6. Study of the influence of resolution and size of the computational domain. Boundary-layer response to free-stream turbulence with $L = 10$. (*a*) $Tu_0 = 2.53\,\%$. Variation of chord- and spanwise resolution of box S; see table 2. $N_x \times N_y \times N_z = 384 \times 121 \times 128$ (——); $512 \times 121 \times 128$ (----); $384 \times 121 \times 192$ (-·-·-). (*b*) $Tu_0 = 3.73\,\%$. Variation of spanwise size of box S. $L_z = 200$ (——); $L_z = 300$ (----).

the original and the modified domains is composed of modes with wavenumbers between $\kappa_l = 0.05$ and $\kappa_u = 1.1$ with a turbulence intensity of $Tu_0 = 2.53\,\%$ and a characteristic length of $L = 10$. It becomes clear from figure 6(*a*) that the receptivity and the subsequent growth of the instability obtained on the coarsest grid do not differ from the results on the two refined meshes.

Next, the influence of the width L_z of the numerical domain on the boundary-layer response is examined. This is investigated by considering the shorter box S with $L_z = 300$ and $N_z = 192$, i.e. the spanwise resolution is kept fixed. For a fair comparison, the parameters defining the free-stream turbulence are left unchanged: the turbulence intensity considered is $Tu_0 = 3.73\,\%$ and the integral length $L = 10$. Figure 6(*b*) shows the downstream evolution of the excited boundary-layer disturbance in the wider domain as well as in box S. The initial transient disturbance growth is slightly enhanced in the wider domain whereas the disturbance growth rate farther downstream is hardly affected. This difference can be explained by the nonlinear interactions occurring between wider structures at the initial receptivity phase. The spanwise scale of the disturbance is not changed by the increased domain size as shown by the identical growth rates downstream. Note, however, that the results are obtained for the second highest free-stream turbulence intensity studied, $Tu_0 = 3.73\,\%$, and the agreement between the curves is expected to improve at lower Tu_0. In light of the rather small influence of L_z on the boundary-layer response and for the sake of the computational costs, the subsequent simulations are performed on the default domain in table 2 with $L_z = 200$.

2.6. *Characterization of the free-stream turbulence*

Because of the distribution of the modal wavenumbers defining the free-stream turbulence on concentric spherical shells, the resulting disturbance field is homogeneous and isotropic. In swept-plate flow with favourable pressure gradient, however, the mean flow is subject to chordwise acceleration ($\partial U/\partial x > 0$). This gives rise to non-zero production terms in the Reynolds-stress transport equation (see for instance Pope 2001). Figure 7 displays the behaviour of the artificial turbulence field in the free stream. In figure 7(*a*), the downstream decay of the total turbulence intensity at three different levels above the plate is plotted. The turbulent inflow conditions are $Tu_0 = 3.73\,\%$ with $L = 10$. It is apparent that the turbulence intensity

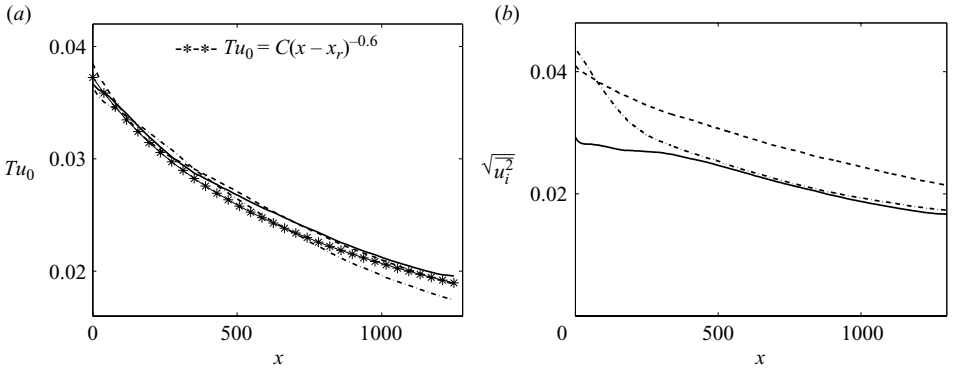

FIGURE 7. Downstream decay of free-stream turbulence with inflow turbulence intensity of $Tu_0 = 3.73\,\%$ and integral length $L = 10$. (a) Downstream evolution of Tu_0 measured at three levels above the plate: $y = 30$ (——); 35 (----) and 45 (-·-·-). Comparison with energy decay characteristic for grid turbulence (-*-*-); see Fransson, Matsubara & Alfredsson (2005). Here, $C = 1.73$ and $x_r = -600$. (b) Decay of the three fluctuation components measured at $y = 40$ for free-stream turbulence with $Tu_0 = 3.73\,\%$. $\sqrt{\overline{u^2}}$ (——); $\sqrt{\overline{v^2}}$ (----) and $\sqrt{\overline{w^2}}$ (-·-·-).

decays at a rate similar to that in homogeneous isotropic turbulence, where the energy decay obeys a power law. In Fransson *et al.* (2005), the exponent of this law has been experimentally determined as -0.6 for grid-generated turbulence, while the parameters C and x_r depend on the turbulence grid. Here, the curve fit has been done with $C = 1.73$ and $x_r = -600$. The plot also shows that the decay rate depends only weakly on the wall-normal level and hence that homogeneity is maintained across the free stream. However, figure 7(b) reveals that the turbulent kinetic energy is not equally distributed among the fluctuation components and their individual decay differs. The adjustment to the free-stream conditions occurs already in the fringe region and in the region near the inflow plane where $\partial U/\partial x$ and the streamline curvature are maximum. The wall-normal fluctuations are larger than their chordwise counterpart. This can be explained by considering the production terms in the Reynolds-stress transport equation for the chordwise u and wall-normal v fluctuations in accelerating flows,

$$\mathscr{P}_{11} = -2\overline{u^2}\frac{\partial U}{\partial x}, \tag{2.10a}$$

$$\mathscr{P}_{22} = -2\overline{v^2}\frac{\partial V}{\partial y} \quad = 2\overline{v^2}\frac{\partial U}{\partial x}. \tag{2.10b}$$

A negative production term is seen in the first equation, whereas positive production of wall-normal fluctuations is caused by the flow acceleration, where the continuity equation has been used to relate the mean-flow gradients. Energy is drained from the u-component of the free-stream turbulence into the v-component by the chordwise acceleration of the underlying mean flow. The spanwise velocity fluctuations, initially strong, decay rapidly until they reach amplitudes similar to those pertaining to u. The relative enhancement of the wall-normal fluctuations can also be related to the stretching of chordwise vorticity, as observed for example in the convergent section of a wind tunnel, while the drop of u and w is associated with the decrease of wall-normal vorticity induced by the negative $\partial V/\partial y$.

Disturbance source	Amplitude	
Free-stream turbulence	$Tu_0 \times 10^2$	0.17; 0.42; 0.84; 1.26; 1.69; 2.11; 2.53; 2.95; 3.73; 5.06
Surface roughness	$\varepsilon_h \times 10^2$	3.75; 7.5; 15

TABLE 3. Amplitude of the forcing disturbance. Turbulence intensity of the free-stream turbulence at the inflow plane and r.m.s. height of the surface-roughness strip.

3. Results

The response of the three-dimensional swept-plate boundary layer to free-stream turbulence and surface roughness is studied. The disturbance amplitude is expressed in terms of the turbulence intensity for the free-stream disturbance and the r.m.s. height for the roughness. The values considered are compiled in table 3. The statistics presented in the following are obtained by averaging in time and in the spanwise direction. Note that the r.m.s. values are indicative of the total disturbance energy, sum of the energy in the modes with different wavenumbers. The phase relation between the individual components, however, determines the local distortion. Therefore, r.m.s. values can mask large localized distortions, the origin of secondary instabilities.

3.1. *Part I. Laminar–turbulent transition*

Results on the transition under a high-amplitude disturbance environment are presented first. The skin-friction coefficient provides a good indication of the transition location. This is shown in figure 8(*a*) for free-stream turbulence with inflow intensities of $Tu_0 = 2.53\,\%$ and $3.73\,\%$. The completion of transition is observed farther upstream when increasing the level of the external disturbance. Bonfigli (2006) pointed out that the skin friction does not exhibit an overshoot before approaching the value for fully turbulent flow, in contrast to the case of Blasius flow (cf. Monokrousos *et al.* 2008, for instance), and this observation is confirmed here. In figures 8(*c*) and 8(*d*), the boundary layer is characterized in terms of displacement and momentum-loss thickness as well as shape factor. These quantities are computed from both the chord- and the spanwise mean flows. A substantial rise of the thicknesses and drop of the shape factor is observed around $x \approx 700$ and $x \approx 900$, respectively, indicating the region of laminar–turbulent transition. In agreement with experimental and numerical findings for bypass transition in two-dimensional boundary layers (Matsubara & Alfredsson 2001; Brandt *et al.* 2004), the displacement thickness is seen to decrease slightly below the laminar values in the transitional region, and then to increase faster in the turbulent flow. The momentum loss is, on the contrary, always larger than in the laminar case owing to the increase of skin friction caused by the occurrence of the turbulent spots. Note in figure 8(*d*) that the shape factor computed from the chordwise mean velocity slightly increases in the laminar region rather than being constant. This shows that the chordwise base-flow profiles, solution to the Navier–Stokes equations, are not exactly self-similar, in contrast to the initial Falkner–Skan profiles.

The wall-normal maximum of the chordwise, wall normal and spanwise velocity fluctuations is reported in figure 8(*b*). Upstream of $x \approx 200$ the v component is weak while the horizontal components rapidly grow. This indicates that the boundary layer is initially subject to non-modal instability, as typically observed in two-dimensional boundary layers. In Blasius flow, only the streamwise velocity component grows at the initial stages of the transition while the cross-stream components decay (Brandt *et al.* 2004). In three-dimensional boundary layers, in contrast, the basic flow is characterized

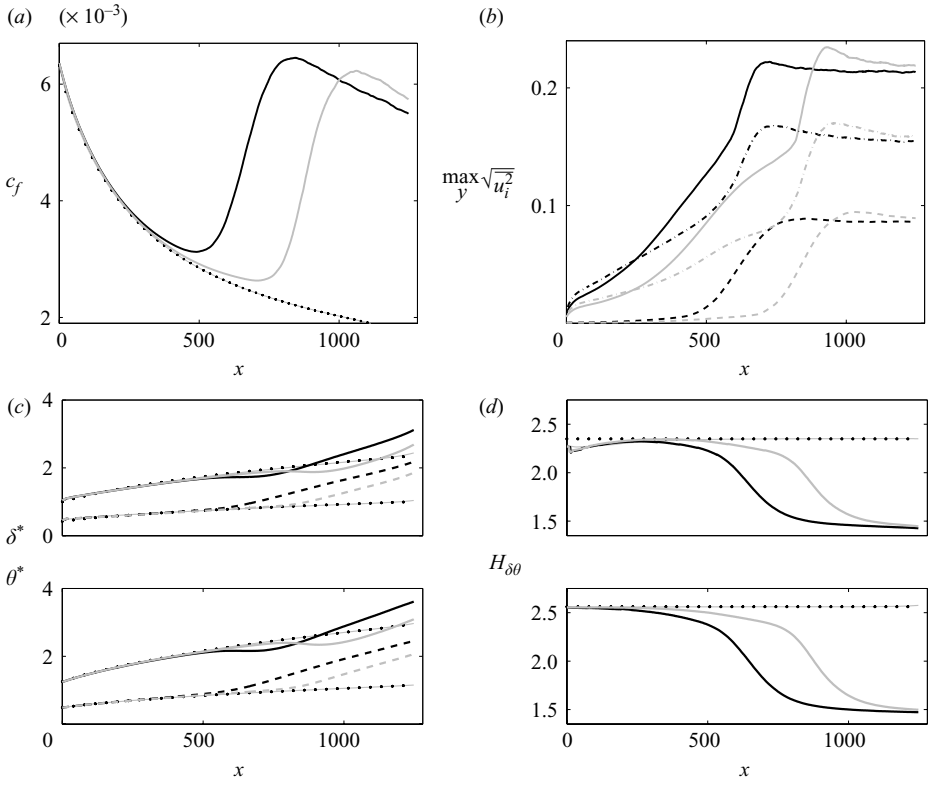

FIGURE 8. Visualization of breakdown to turbulence of swept-plate flow exposed to free-stream turbulence with inflow turbulence intensity of $Tu_0 = 2.53\,\%$ (grey) and $3.73\,\%$ (black) through (a) skin-friction coefficient and (b) downstream evolution of the r.m.s. of chordwise (——), vertical (----) and spanwise disturbance velocities (-·-·-·-). (c) Evolution of displacement (——) and momentum-loss thickness (----) and (d) shape factor, based on chord- (top) and spanwise mean velocity (bottom). The laminar solution (thin grey) and the theoretical curves for Falkner–Skan–Cooke flow (dots) are given as well.

by wall-normal shear in both the chordwise and spanwise directions; therefore, the lift-up effect induces the growth of both components, as observed in the figure. Upstream transient growth is thus found to be a precursor of downstream crossflow modes, providing crossflow modes with initial energy. After the initial phase of primary growth, a fast increase in the amplification rate is observed in figure 8(b) first for the case with $Tu_0 = 3.73\,\%$, $x \approx 600$, and later for the lower intensity $Tu_0 = 2.53\,\%$, $x \approx 800$. This is associated with the rapid rise in skin-friction coefficient in figure 8(a) and is due to the appearance of high-frequency secondary instabilities and turbulent spots in the flow. The weak overshoot in the curves for the velocity fluctuations can be related to the maximum values of skin friction. The maximum amplitude prior to breakdown is slightly larger for $Tu_0 = 2.53\,\%$ than that for $Tu_0 = 3.73\,\%$, i.e. the breakdown is not initiated at the same disturbance level inside the shear layer. This suggests that the transition location can only approximately be predicted from a certain threshold amplitude of the primary crossflow mode alone. At the end of the computational domain, the level of velocity fluctuations is almost the same for the two cases: the flow has reached an equilibrium turbulent state.

It is worth pointing out the difference between the disturbance evolution depicted in figure 8(*b*) and, for instance, the data in figure 10(*a*) of Fransson *et al.* (2005) pertaining to non-modal growth of streaks in two-dimensional boundary-layer flow. Fransson *et al.* (2005) report a strong overshoot in the curves for the streamwise fluctuation energy, intensifying with increasing Tu, before the energy level sets to a constant value in the fully turbulent boundary layer. This behaviour suggests a pronounced region of intermittency in two-dimensional flow, which is not observed here in the swept boundary layer. This discrepancy can be explained with the different dominating instability types prior to transition: the crossflow vortices in swept flow are destabilized much faster by secondary instability than the streaks in two-dimensional flow. Therefore, the amplitude of the crossflow modes (upon nonlinear saturating effects) and the average transition location may be more closely correlated in three-dimensional boundary layers than in their two-dimensional counterpart.

An overall picture of the transition in swept boundary layers exposed to free-stream turbulence is provided in figure 9. This figure displays a time series of snapshots of the flow in a wall-parallel plane inside the boundary layer, $y = 2$, together with a view of the free-stream fluctuations in a plane located at $y = 40$ well above the boundary layer, figure 9(*a*). The results are obtained with inflow turbulence of intensity $Tu_0 = 3.73\,\%$ and length scale $L = 10$, and the snapshots are taken after the flow field has reached a statistically converged state. The flow is swept from left to right and bottom to top in the figure. As seen in figure 9(*a*), the finer length scales of the external disturbance disappear farther downstream, indicating decay of the free-stream turbulence. Figures 9(*b*)–9(*g*) show that instabilities in the laminar region of the boundary layer appear in the form of long structures, tilted about 45° with respect to the chord of the plate. Around $x = 500$, these structures have reached a threshold amplitude such that the boundary layer becomes susceptive to secondary instabilities: high-frequency modes are triggered at random locations and grow rapidly in amplitude. Instabilities are most likely triggered by high-frequency components of the free-stream turbulence. An alternative mechanism may be the nonlinear interaction between low-frequency modes already in the boundary layer (see also Brandt & de Lange 2008, for two-dimensional flow).

Patches of irregular motion are seen to appear farther downstream, forming local regions of turbulence called spots. The spot seen in figure 9(*b*) grows in size with time; a second spot occurs in figure 9(*c*) and both spots become wider and longer as they travel downstream. At time $t = 6230$ (figure 9*e*), a third spot can be identified in the lower part of the domain and later (figure 9*g*), the three turbulent spots have almost merged to form one large region of turbulent motion. Downstream of $x = 700$ the boundary layer is fully turbulent, and the turbulent region is constantly fed by merging spots incident from the upstream laminar part of the layer. It becomes apparent that the dominant disturbance structures in the fully turbulent boundary layer are still elongated and tilted in the free-stream direction (Schlatter & Brandt 2008). Note, finally, that all spots in figure 9 form in a rather limited chordwise region. This provides further indication for a less pronounced intermittency phase of this transition scenario as compared with bypass transition in the two-dimensional flow.

Figure 10 characterizes the wall-normal and spanwise length scales of the disturbance structures inside the boundary layer by showing contour lines of instantaneous chordwise velocity in lateral planes at four downstream locations. At $x = 300$ (figure 10*a*), the deformation of the mean flow is still moderate, and the smallest observed spanwise length scale is about 10, i.e. comparable to the

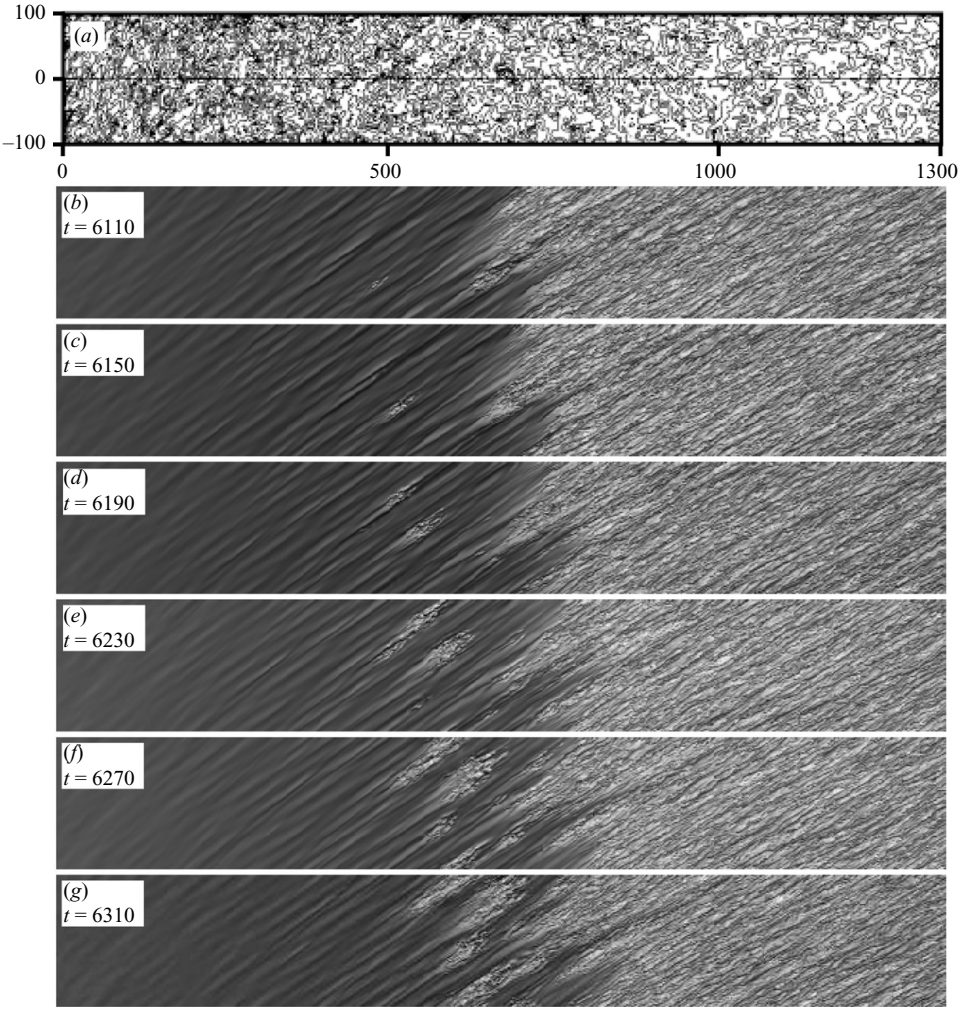

FIGURE 9. Free-stream turbulence with intensity $Tu_0 = 3.73\,\%$ and integral length $L = 10$ and the response of the swept-plate boundary layer to it. The flow is from left to right. (a) Downstream evolution of the chordwise fluctuation u in the free stream at $y = 40$. (b–g) Boundary-layer response in terms of the chordwise fluctuation u at $y = 2$ at different instants of time.

integral length scale of the free-stream turbulence. Farther downstream, at $x = 400$ and 500, contour lines typical for crossflow modes are identified, the gradients in instantaneous chordwise velocity have become steeper and the structures have grown in size in the wall-normal direction with the boundary layer. Their spanwise size has, in contrast, decreased relative to the layer thickness; see figures 10(b) and 10(c). Owing to the noisy environment and random superposition of different modes, the mean flow deformation does not resemble that usually observed under controlled disturbance generation. Crossflow modes of different amplitude, spanwise and wall-normal scales appear side by side in an unpredictable fashion. However, the formation of strong shear layers supporting rapid secondary instabilities is clearly observed. In figure 10(d), regions of strong flow deformation, steep velocity gradients and fine spanwise scales are identified near the edges of the depicted domain, while the flow

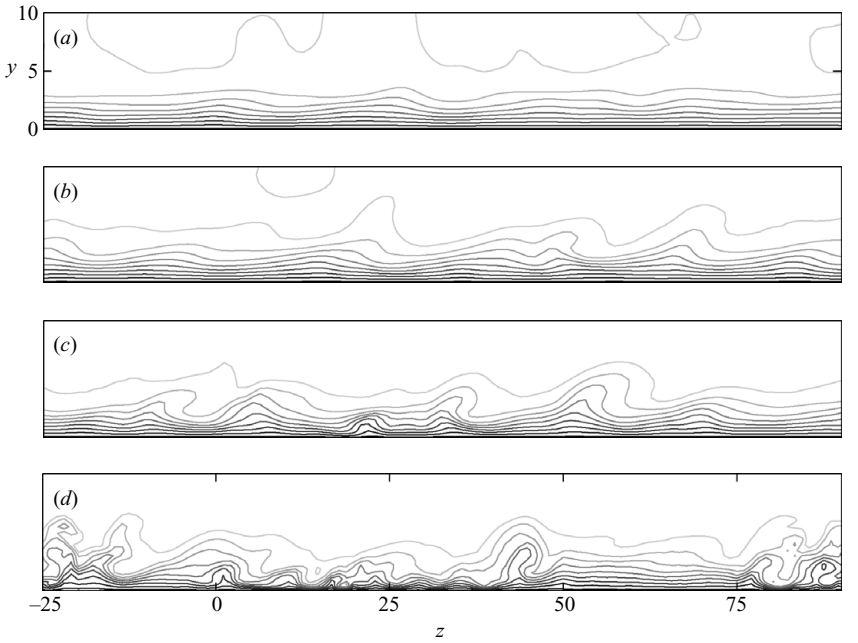

FIGURE 10. Boundary-layer response to free-stream turbulence with intensity $Tu_0 = 3.73\,\%$ and integral length $L = 10$. y–z planes showing contour lines of instantaneous chordwise velocity in the boundary layer for time $t = 6270$ (compare with figure 5*f*) at four chordwise stations upstream of the breakdown location. (*a*) $x = 300$, (*b*) $x = 400$, (*c*) $x = 500$ and (*d*) $x = 600$. The contour lines show levels between 0.05 and 1.25 (from black to grey) with spacing 0.15. Note that the y axis is enlarged by a factor of 1.67.

field in the neighbourhood is smoother. These highly perturbed regions are referred to as turbulent spots (cf. figure 9*f*) and indicate where the boundary layer first approaches the turbulent state. Note that these turbulence patches are located closer to the wall than the original crossflow modes. As in two-dimensional boundary layers, the late-stage high-frequency instability moves from the upper part of the boundary layer towards the wall (Jacobs & Durbin 2001; Brandt *et al.* 2004; Zaki & Durbin 2005).

Next, the disturbance structures caused by the secondary instabilities shortly upstream of the transition location are examined. Secondary instability of crossflow modes has been considered theoretically (Malik *et al.* 1999), experimentally (White & Saric 2005, more recently) and numerically (Bonfigli & Kloker 2007, for a comparison with stability analysis). These instabilities are of inviscid inflectional type and associated with strong shear layers of the mean flow induced by saturated crossflow modes. Following Malik *et al.* (1999), three different classes of modes are identified: (i) mode I or '*z*', associated with the minimum of the spanwise gradient of the streamwise velocity and characterized by high-frequency oscillations; (ii) mode II or '*y*', associated with the maximum of the wall-normal gradient, also characterized by high-frequency oscillations; (iii) mode III, associated with the maximum of the spanwise gradient, characterized by lower frequencies and located closer to the wall. These modes have been clearly identified when considering secondary modal stability of saturated steady crossflow modes, whereas a less clear-cut distinction has been observed for travelling waves, which are more relevant for the transition scenario in

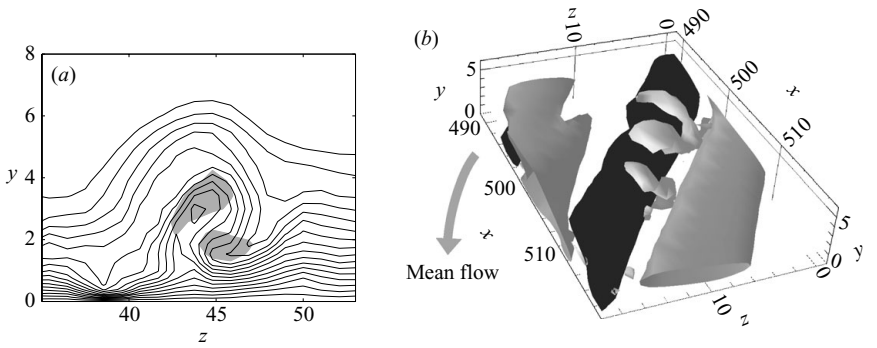

FIGURE 11. Instantaneous flow field upstream of the transition location ($t = 6270$, $Tu_0 = 3.73\,\%$). (a) The y–z plane ($x = 600$) showing contour lines of chordwise velocity with levels between 0.08 and 1.28 and spacing of 0.08. The shaded areas identify regions of high-intensity secondary disturbances (chordwise component). (b) Contours of positive and negative chordwise disturbance velocity (grey: $u = 0.12$; black: $u = -0.12$ and of λ_2 (light grey: $\lambda_2 = -1.4 \times 10^{-3}$).

the presence of free-stream turbulence. A combination of modes 'z' and 'y' seems to appear in the experiments reported by Bippes (1999) under natural conditions.

To identify the relevant flow structures of the spot precursors, numerous velocity fields have been examined in detail. Note that the identification of the various secondary instability modes of travelling crossflow vortices presented by Wassermann & Kloker (2003) required a spanwise Galileian transformation to travel with the primary wave and an adapted temporal–spanwise Fourier decomposition of the disturbance (see the above reference for details). Such an analysis is impossible in the case of disturbances randomly induced by free-stream turbulence. The primary crossflow modes are periodic neither in time nor in space; they appear as elongated structures of finite length. Similarly, the high-frequency perturbations leading to formation of turbulent spots appear as localized, rapidly amplifying wave packets. As a consequence, a visual analysis is adopted to characterize the late stages of the laminar–turbulent breakdown.

An example of typical pre-transitional disturbance structures is provided in figure 11. Figure 11(a) is a close-up of figure 10(d) displaying contour lines of instantaneous chordwise velocity typical for a saturated crossflow vortex. In addition, regions of the most intense secondary perturbation riding on top of the crossflow vortex are shown as shaded areas. These are obtained by following the primary instability mode over a short downstream distance and correlating the instantaneous chordwise velocity at two locations $\vec{x}_1$ and $\vec{x}_2$, $\overline{u(\vec{x}_1)u(\vec{x}_2)}/u^2(\vec{x}_1)$. The perturbation determined in this way represents streamwise fluctuations of the chordwise velocity component along the crossflow vortex. The fluctuations will inevitably also contain the streamwise variation of the underlying primary mode due to non-parallel effects and inhomogeneities; however, this contribution turns out negligible when considering only the regions of largest disturbance.

In the figure, two regions are identified, where the chordwise component of the secondary disturbance velocity is larger than 50 % of the maximum. These two areas can be related (i) to strong shear at the updraught side of the primary vortex in what appears as a combination of modes 'z' and 'y' and (ii) to the region of positive spanwise gradient located closer to the wall, as typically observed for mode III. The

first type of high-frequency perturbation is observed to appear more frequently and to dominate during the breakdown. This can be explained by the fact that the secondary instability is most likely triggered by high-frequency disturbances in the free stream: modes located in the upper part of the boundary layer are thus most easily excited. Note, in addition, that largest growth rates are obtained for modes 'z' and 'y' when examining the linear instability of individual steady crossflow modes or their packets (Wassermann & Kloker 2002).

Finally, vortical structures typical of spot precursors are displayed in figure 11(b). These are identified by the λ_2 criterion (Jeong & Hussain 1995). Finger vortices located on the updraught side of the primary vortex are clearly visible, in agreement with previous numerical studies with controlled disturbances (Wintergerste & Kleiser 1997; Wassermann & Kloker 2002, 2003). Typically, packets of two to three vortices are observed in our simulations.

3.2. *Part II. Receptivity*

First, synthetic turbulence with different intensities is prescribed at the inflow plane of the computational domain, from where it is convected by the free stream while decaying. This disturbance source will occupy the entire free stream and, therefore, act non-locally on the boundary layer. Secondly, a thin roughness strip with a step-like contour in x and a random shape in z direction is placed parallel to the leading edge near the inflow plane of the domain. This disturbance is confined to a small downstream region and hence interacts locally with the boundary layer. Finally, we combine both disturbance sources to determine whether steady or unsteady modes dominate the boundary-layer response. The following results are obtained on the short domain, box S, sufficiently long to include receptivity, primary disturbance growth and nonlinear interaction even for the lowest amplitudes of the forcing disturbance.

3.2.1. *Response to free-stream turbulence*

Figure 12 depicts the downstream evolution of the boundary-layer disturbance forced by free-stream turbulence with different intensities in the range $Tu_0 \in [0.17, 5.06]$ %. Here, Tu_0 is defined by its value at the inflow plane. In figures 12(a) and 12(b), the wall-normal maximum of the r.m.s. of the chordwise fluctuation u is shown versus x for increasing inflow turbulence intensities. The results pertaining to the lower turbulence intensities are reported in figure 12(a) and those for the higher free-stream turbulence levels are reported in figure 12(b) with the curve obtained at lowest Tu_0 repeated for comparison. Initially, $x \lesssim 100$, the instability growth is dominated by transient behaviour, followed by a region of exponential growth. The linear regime extends nearly throughout the whole domain for weak free-stream perturbations with $Tu_0 = 0.17$ % and $Tu_0 = 0.42$ %, whereas the curves obtained in a disturbance environment of higher intensity start to bend off for $x > 400$. This indicates that nonlinear interaction becomes relevant for $Tu_0 > 0.42$ %, causing saturation of the primary disturbances. At the highest inflow turbulence levels of $Tu_0 = 3.73$ % and 5.06 %, secondary instabilities occur within the short computational domain, as apparent by the upward bending growth curves for $x \gtrsim 600$ ($Tu_0 = 3.73$ %) and $x \gtrsim 400$ ($Tu_0 = 5.06$ %). Moreover, breakdown of the laminar boundary layer is observed for $Tu_0 = 5.06$ % at $x \approx 550$. The extent of the linear growth region and the onset of nonlinear behaviour becomes more distinct in figures 12(c) and 12(d), where the curves of figures 12(a) and 12(b) are shown after rescaling the disturbance amplitudes with the inflow turbulence intensity. Clearly, the initial disturbance amplitude and the incipient transient growth scale with Tu_0 for all intensities under

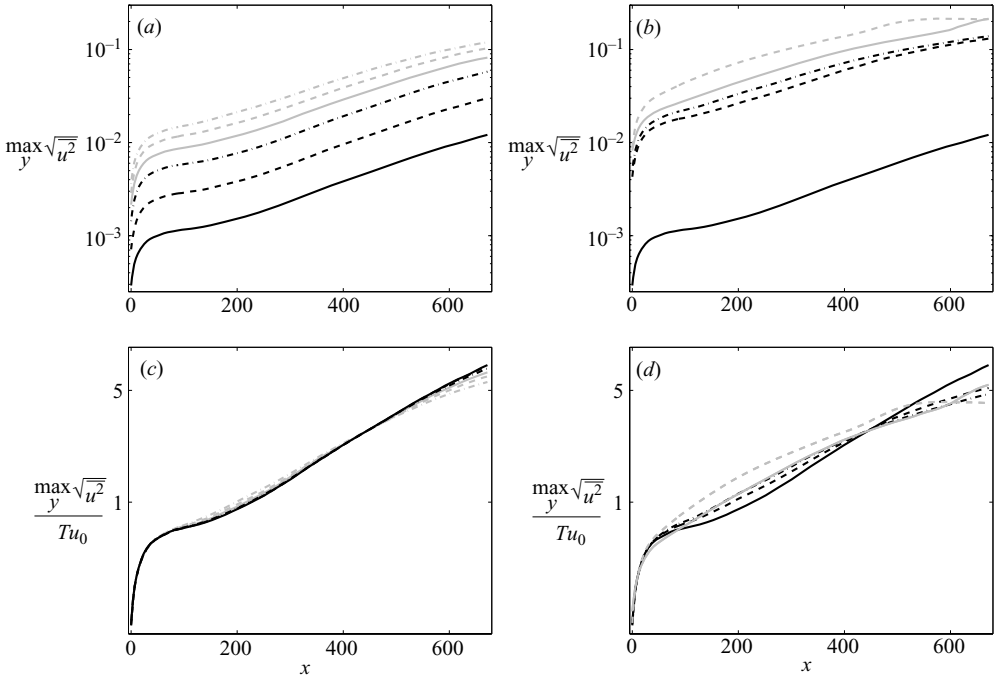

FIGURE 12. Boundary-layer response to free-stream turbulence with integral length $L = 10$ and different intensities: (*a*) $Tu_0 = 0.17\,\%$ (black ——); $0.42\,\%$ (black ----); $0.84\,\%$ (black -·-·-); $1.26\,\%$ (grey ——); $1.69\,\%$ (grey ----) and $2.11\,\%$ (grey -·-·-). (*b*) $Tu_0 = 0.17\,\%$ (repeated for comparison; black ——); $2.53\,\%$ (black ----); $2.95\,\%$ (black -·-·-); $3.73\,\%$ (grey ——) and $5.06\,\%$ (grey ----). (*c*) The data from (*a*) scaled with the inlet turbulence intensity Tu_0 and (*d*) the curves from (*b*) scaled by Tu_0.

investigation, indicating that the receptivity process is linear. In particular, the first data point at $x = 0$ can be interpreted as receptivity coefficient based on Tu_0: here, a value of about 0.2 is obtained. At the lower intensities in figure 12(*c*), the primary instability growth depends linearly on Tu_0 in the region $x \lesssim 450$, while saturation of the amplitude sets in farther downstream. The present results also suggest that the individual instability modes evolve independently for turbulence intensities $Tu_0 \lesssim 2\,\%$. Figure 12(*d*) reveals that the curves obtained at higher intensities ($Tu_0 \geqslant 2.53\,\%$) do not collapse as well with the data for $Tu_0 = 0.17\,\%$, showing that the dependence of the primary instability evolution on the incoming turbulence intensity becomes nonlinear at the highest levels of Tu_0. The larger amplification observed is most likely due to nonlinear forcing among unsteady low-frequency modes with different spanwise scales rather than to a different behaviour of the free-stream turbulence when Tu_0 is large (e.g. nonlinear interaction in the free stream).

The receptivity mechanism to free-stream turbulence can be summarized as follows. The upstream disturbance, undergoing non-modal growth because of the excitation and interaction of a vast number of scales, soon evolves into an exponential disturbance composed of unstable crossflow modes. This suggests that the receptivity mechanism is active in the upstream part of the boundary layer; farther downstream the crossflow modes develop rather independently from the free stream until the onset of secondary instability. Schrader *et al.* (2009) demonstrate, in fact, that receptivity to free-stream vortical disturbances like those used here is in particular relevant near

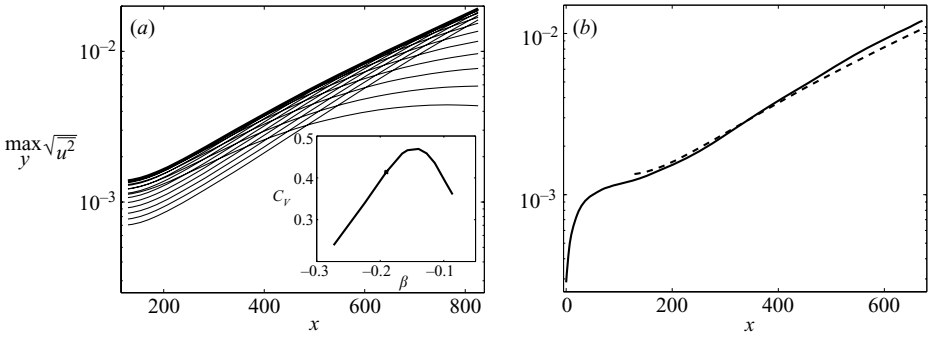

FIGURE 13. Boundary-layer response to forcing with free-stream turbulence of $Tu_0 = 0.17\,\%$. (*a*) Growth of crossflow modes with angular frequency $\omega = -0.01$ and various spanwise wavenumbers in the range $(-0.27,-0.09)$ obtained through the PSE method (——, thin). The curves are weighted with the corresponding receptivity coefficients (insertion from Schrader *et al.* 2009). The envelope curve is also shown (——, thin). (*b*) Boundary-layer response for $Tu_0 = 0.17\,\%$ (——) in comparison with the envelope curve from (*a*) (----).

the leading edge where the length scales of the unstable crossflow modes are most efficiently generated by a scale-conversion mechanism; thus, the receptivity depends on the inflow location of the simulation. This points to the need of including the leading-edge region in order to exactly capture the receptivity of the shear layer to free-stream turbulence, which is beyond the scope of this work.

The existence of different spanwise wavenumbers β and angular frequencies ω in the free stream leads to the excitation and competition between unstable crossflow modes with different β and ω, growing at different rates and becoming dominant at different downstream locations. Therefore, the curves for the evolution of the boundary-layer instabilities in figure 12 do not exhibit a clean exponential behaviour; instead, they represent the envelope for the evolution of individual unstable crossflow waves. Figure 13(*a*) provides data for the downstream development of the amplitude of a number of unstable modes with $\omega = -0.01$ and with various spanwise wavenumbers β. Note that β and ω of the most unstable crossflow modes take negative values for the reference system and modal ansatz function adopted, while the streamwise wavenumber α is positive. The curves are obtained through the solution of the PSE. As the receptivity is not included in the PSE framework, the evolution curves need to be weighted with the corresponding receptivity coefficients. Here, the coefficients for vortical free-stream disturbances from Schrader *et al.* (2009) (inset of figure 13*a*) are used. To obtain the total amplitude of the boundary-layer disturbance, the envelope of the weighted amplitude-evolution curves is computed and compared with the present results from the full nonlinear simulation; see figure 13(*b*). Although the envelope curve only includes crossflow modes with frequency $\omega = -0.01$, it provides a good approximation of the actual disturbance growth observed in the simulations. This demonstrates, on the one hand, that low frequencies like $\omega = -0.01$ play a major role during the receptivity process and, on the other hand, that the receptivity coefficients computed by Schrader *et al.* (2009) for vortical free-stream disturbances of single wavelength also properly describe receptivity to free-stream turbulence. Note that larger growth rates downstream may be obtained when including modes with lower frequency.

Next, we investigate the characteristic size and spacing of the boundary-layer instability structures. In figure 14, the spacing Δz between the disturbance structures in

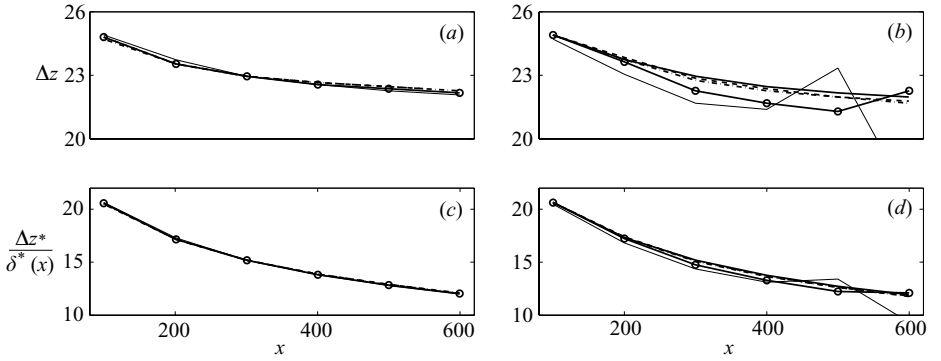

FIGURE 14. Characteristic spanwise spacing between the disturbance structures excited by free-stream turbulence at various intensities. (*a*) $Tu_0 = 0.17\,\%$ (——); 0.42 % (----); 0.84 % (-·-·-); 1.26 % (-○–○-); 1.69 % (——, thin) and 2.11 % (----, thin). (*b*) $Tu_0 = 0.17\,\%$ (——); 2.53 % (----); 2.95 % (-·-·-); 3.73 % (-○–○-) and 5.06 % (——, thin). (*c*, *d*) The same data as in (*a*) and (*b*), respectively, but Δz is normalized by the local instead of the inflow displacement thickness.

the region of primary instability growth is displayed versus the chordwise coordinate. The spacing Δz is determined by computing the spanwise two-point correlations $\overline{u(z)u(z+\Delta z)}/\overline{u^2(z)}$ for the chordwise fluctuation u and is defined as twice the location Δz_{min} of the first minimum of the obtained correlation curve, $\Delta z(x) = 2\Delta z_{min}(x)$. It can be interpreted as the spanwise spacing between two adjacent instability structures with a disturbance velocity in the same direction, for instance two contiguous crossflow modes or two high-speed streaks. Figure 14(*a*) shows the characteristic spacing obtained under turbulence with $Tu_0 \leqslant 1.69\,\%$, revealing that Δz is independent of Tu_0 in this range and that it slowly drops downstream. In figure 14(*b*), a slightly faster decrease of the spacing is observed for the more intense free-stream fluctuations, in particular for the two largest values of $Tu_0 = 3.73\,\%$ and 5.06 %. This is in line with the experimental findings of Matsubara & Alfredsson (2001) for the two-dimensional boundary layer exposed to turbulence from grid B, where the downstream decrease in spacing has been reported to be slower under free-stream turbulence of low intensity than in high-level turbulence. The rapid drop in Δz for $Tu_0 = 5.06\,\%$ downstream of $x = 500$ reveals that breakdown to turbulence is observed within the domain for this case: the disturbance structures rapidly break up into smaller scales in this region. Upstream of the breakdown location, Δz increases somewhat before it finally drops. This increase is also seen at the second highest turbulence intensity of $Tu_0 = 3.73\,\%$, indicating imminent transition. In figures 14(*c*) and 14(*d*), the data from figures 14(*a*) and 14(*b*) are rescaled with the local displacement thickness instead of its inflow value. These figures demonstrate that the characteristic size of the primary instability decreases relative to the local size of the boundary layer for all values of Tu_0.

3.2.2. *Response to surface roughness*

Steady surface roughness provides an efficient receptivity mechanism for stationary crossflow vortices (e.g. Crouch 1993; Choudhari 1994). Here, a chordwise localized spanwise surface-roughness strip with the shape shown in figure 3(*b*) is placed on the plate near the inflow plane of the computational domain, while the free stream is now disturbance free. Roughness elements with different r.m.s. heights are considered: $\varepsilon_h = 0.0375$, 0.075 and 0.15. The total perturbation induced by the roughness strip will be distributed among the 16 spanwise wavenumbers included in the bump shape

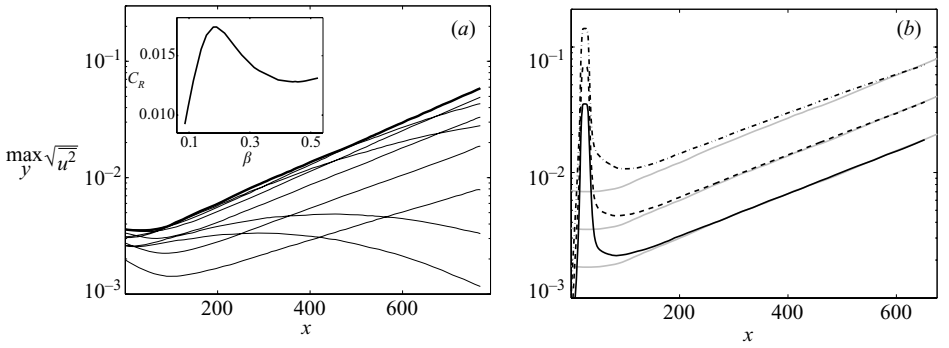

FIGURE 15. Boundary-layer response to forcing through a random surface-roughness strip. (*a*) Growth of steady crossflow modes with various spanwise wavenumbers in the range (−0.47,−0.097) (——, thin). The curves are from Schrader *et al.* (2009) and weighted with the corresponding receptivity coefficients from the same reference (insertion). The envelope curve is also shown (——, thick). (*b*) Boundary-layer response for $\varepsilon_h = 0.0375$ (——), $\varepsilon_h = 0.075$ (----) and $\varepsilon_h = 0.15$ (-·-·-) in comparison with the envelope curve from (*a*) (grey).

such that the individual modal amplitudes are lower. The present roughness elements can be considered as low-amplitude roughness. Because of the forcing at various wavelengths, different crossflow waves will appear and compete with each other. Figure 15 shows the response of the shear layer to the roughness. In figure 15(*a*), the growth of various steady crossflow modes with spanwise wavenumbers included in the lateral contour of the roughness strip is depicted. The curves are weighted with the receptivity coefficients from Schrader *et al.* (2009) and their envelope is compared with the downstream evolution of the disturbance amplitude from the present nonlinear simulations (figure 15*b*). The envelope is dominated by the crossflow mode $\beta = -0.22$, the mode of strongest receptivity among those forced in the simulation. The agreement between the envelope and the evolution curve for the layer disturbance is good for $\varepsilon_h = 0.0375$ and 0.075, revealing that the receptivity coefficients computed within the linear approximation and for the simplified roughness model of Schrader *et al.* (2009) are also valid for receptivity to the random roughness strip considered here. Nonlinear interaction between the forced crossflow waves is not significant, and the disturbance growth exhibits a rather clean exponential behaviour. It is concluded that both roughness receptivity and the subsequent disturbance growth are linear for the two lower values of ε_h: the solid curve ($\varepsilon_h = 0.0375$) in figure 15(*b*) collapses with the dashed line ($\varepsilon_h = 0.075$) when multiplied by 2. If the height of the roughness strip is further increased to $\varepsilon_h = 0.15$, nonlinear effects become visible downstream of the roughness. The disturbance amplitude just downstream of the bump becomes larger than twice that for $\varepsilon_h = 0.075$. Since it has been shown by Schrader *et al.* (2009) that receptivity is still linear in ε_h for $\varepsilon_h = 0.15$, we ascribe the behaviour seen in figure 15(*b*) to the downstream nonlinear interaction of linearly excited modes. Finally, the disturbance amplitude bends downward for $x \gtrsim 500$, indicating saturation due to nonlinearity.

3.2.3. *Response to free-stream turbulence with surface roughness*

It is of interest to determine which type of disturbance—steady or unsteady crossflow vortices—dominates inside the layer and causes the breakdown to turbulence. This issue has so far been addressed only through wind-tunnel experiments; see the review by Saric *et al.* (2003). In Schrader *et al.* (2009), a numerical analysis involving the combination of simplified models for free-stream

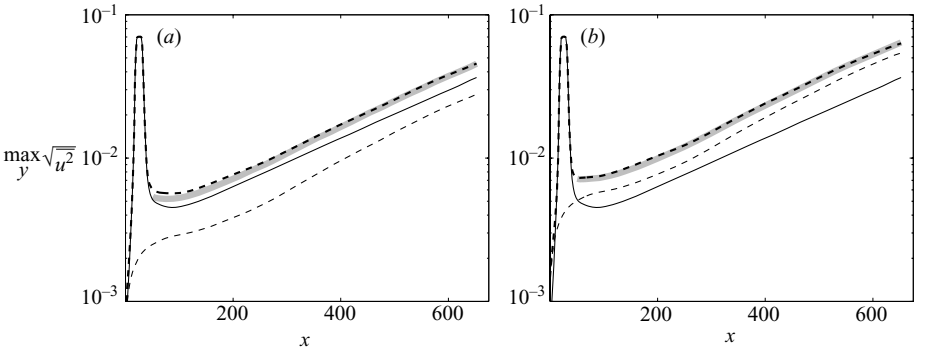

FIGURE 16. Swept-plate boundary layer exposed to turbulent fluctuations of (*a*) $Tu_0 = 0.42\,\%$ and (*b*) $Tu_0 = 0.84\,\%$ and to a localized wall-roughness strip with r.m.s. amplitude $\varepsilon_h = 0.075$. The thin black curves represent the unsteady (----) and the steady disturbance evolution (——) due to turbulence and roughness alone. Their sum (thick grey ——) is compared with the total disturbance (black ----) observed in the simulations with combined perturbation sources.

vorticity and roughness is presented. The threshold in turbulence intensity, above which travelling crossflow instability dominates over stationary disturbance waves, has been estimated to $Tu_0 = 0.5\,\%$. Here, we use more complex representations for free-stream turbulence and surface roughness and examine the response of the swept boundary layer to different combinations of the amplitudes Tu_0 and ε_h of free-stream turbulence and roughness. Tu_0 is varied while the roughness height is kept fixed at $\varepsilon_h = 0.075$. This value is larger than those in the experiments by Reibert *et al.* (1996) ($\varepsilon_h \approx 0.025$), where the roughness has, however, a dominant spanwise length scale. Note that the threshold beyond which the predominant crossflow waves are unsteady is dependent on the roughness height chosen.

The results from two simulations differing in the inflow intensity Tu_0 of the turbulent free-stream fluctuations are shown in figure 16: $Tu_0 = 0.42\,\%$ in figure 16(*a*) and $0.84\,\%$ in figure 16(*b*). The amplitude of the roughness strip is identical in both cases ($\varepsilon_h = 0.075$). The evolution of the boundary-layer disturbance obtained in the presence of both perturbation sources is displayed together with the development of the perturbation induced by free-stream fluctuations and wall roughness alone. In figure 16(*a*) steady crossflow modes dominate over travelling waves, while the situation is vice versa at larger free-stream turbulence intensity as shown in figure 16(*b*). It can, thus, be concluded that the threshold, above which unsteady modes become significant, is passed in the region $0.42\,\% < Tu_0 < 0.84\,\%$, when the roughness height is $\varepsilon_h = 0.075$. The estimate from Schrader *et al.* (2009) is within this range. Figure 16 further reveals that the total shear-layer disturbance in the simulations with combined perturbation sources can be correctly estimated by summing the unsteady and the steady contribution. This observation holds in the steady-wave-dominated case in figure 16(*a*) as well as in the travelling-mode-dominated situation in figure 16(*b*). The interaction between the travelling and the stationary disturbances appears to be negligible for the present configuration and an accurate prediction of the boundary-layer response can be obtained by considering both disturbance sources independently.

4. Discussion and conclusions

Receptivity, disturbance growth and breakdown in three-dimensional boundary-layer flow developing on a swept plate under a favourable pressure gradient have been

investigated. The flow has been perturbed by free-stream turbulence, a roughness strip with spanwise random amplitude and the combination of both. Under the conditions studied, both disturbance sources efficiently excite crossflow vortices.

In the first part of the paper, the route of laminar–turbulent transition is illustrated by describing the disturbance structures dominating during the different stages of transition. Although there exist publications on wind-tunnel experiments of swept-plate flow (e.g. Bippes 1999), the present work is to our knowledge the first that presents a numerical simulation of crossflow-mode-dominated transition in swept-plate flow with free-stream turbulence. Numerical studies on transition initiated by controlled wall disturbances are, in contrast, already available for both steady and travelling crossflow instabilities (Wassermann & Kloker 2002, 2003). Our study reveals that, owing to their large amplification rate, the crossflow modes dominate the disturbance environment of the boundary layer prior to the breakdown. This is in contrast to two-dimensional boundary layers, where T-S waves are irrelevant compared to non-modal streaks already for moderate levels of external turbulence. However, we speculate that non-modal disturbances become more relevant in three-dimensional boundary layers when decreasing the sweep angle and the free-stream acceleration. With only roughness the dominant pre-transitional structures are steady crossflow vortices. Although transient behaviour is observed in the vicinity of the roughness, non-modal disturbances do not play any significant role in this case.

Unlike the breakdown of streamwise streaks in two-dimensional boundary layers (Fransson *et al.* 2005), transition in three-dimensional laminar flow is characterized by a low intermittency between laminar and turbulent flows. An analysis of instantaneous velocity fields confirms that turbulent spots indeed originate in a narrower streamwise region than in Blasius flow. In addition, simulations with different external perturbations show that transition occurs when the level of velocity fluctuations inside the boundary layer reaches similar threshold values. These facts indicate that breakdown is triggered by rapid secondary instability of the crossflow modes and that transition–prediction models may be based on a critical threshold amplitude of the primary disturbance, as suggested by Poll (1984) (see also Wassermann & Kloker 2002). Poll (1984) suggests to correlate the onset of secondary instabilities to a local Reynolds number variation related to the local mean flow deceleration and the wall distance of the location of the maximum negative spanwise gradient. However, so far a critical value for this Reynolds number variation has not been established for the case of travelling modes (Wassermann & Kloker 2003). To predict where the critical threshold amplitude of the crossflow modes has reached, computations will also have to include nonlinear saturating effects, the PSE method probably being the most suited candidate. Such calculations will not be useful, though, unless a correct initial amplitude for the instability mode is provided. This is the aim of the receptivity analysis discussed next.

The second part of the paper focuses on receptivity and the early stages of primary disturbance growth in the swept-plate boundary layer. The results indicate that the initial amplitude of the instability modes scales linearly with the free-stream turbulence intensity. Larger downstream amplification induced by nonlinear forcing among unsteady modes of low frequency and different spanwise scales is observed for free-stream turbulence intensities $Tu_0 \gtrsim 2\,\%$. Above this level, the amplitude of the shear-layer perturbation cannot be correctly estimated only by considering the evolution of individual modes. Furthermore, the receptivity coefficients from Schrader *et al.* (2009) for simplified vortical disturbances have been applied here and compared with the amplification observed in the present, fully nonlinear simulations. This is, in

practice, done by weighting the evolution of the various excited unstable modes with their individual receptivity coefficients and computing the envelope curve. Although the linear receptivity model of Schrader *et al.* (2009) accounts for one—however, dominant—angular frequency only, good agreement between the amplification from the present simulations and the envelope has been found for the case of free-stream turbulence. This confirms that the receptivity mechanisms for the different excited unsteady modes are independent of each other for moderate turbulence levels and that linear receptivity models are also valid for receptivity to complex free-stream turbulence fields. This conclusion can also be drawn for receptivity to localized roughness with spanwise random amplitude. Whereas the receptivity mechanism has been found to be linear even for the highest considered roughness (15 % of the local displacement thickness), nonlinear interaction between the excited steady modes soon sets in downstream of the highest roughness. It is concluded that the onset of nonlinear interaction of the triggered modes is found for roughness heights between 7.5 % and 15 % of the boundary-layer displacement thickness.

Finally, the co-existence of unsteady and steady crossflow vortices has been studied, when free-stream turbulence acts on the boundary layer over a wall with localized roughness. Stationary crossflow vortices dominate the pre-transitional boundary layer when the intensity of the free-stream turbulence is low (see also Saric *et al.* 2003): for low-amplitude roughness (7.5 % of the local displacement thickness) and a turbulence intensity of 0.42 %, the total boundary-layer disturbance is dominated by the steady contribution due to roughness, while at a turbulence level of 0.84 % unsteady crossflow instability is more energetic than the steady modes. Even in the presence of two distinct disturbance sources where nonlinear interaction may be expected, a correct prediction of the evolution of the boundary-layer perturbations can be obtained by investigating the development of individual crossflow modes. This conclusion holds for amplitudes at which the changeover between steady- and travelling-mode-dominated transitions is identified. However, the experimental investigations reviewed by Bippes (1999) suggest that the simultaneous presence of different crossflow modes may affect the late stages of breakdown. This remains an open issue worthy of further analysis.

In summary, our results suggest that receptivity coefficients from simplified models like those proposed by Schrader *et al.* (2009) can be combined with established transition-prediction tools such as the e^N-method or more advanced approaches based on a critical threshold amplitude of the primary instability. This presumes the exact knowledge of the receptivity coefficients for the disturbances relevant in the flow of interest. Simplified approaches, for instance the method based on finite-Reynolds number theory (FRNT; e.g. Crouch 1992; Choudhari 1994), may for many flow types prove accurate enough to establish receptivity coefficients for different disturbance conditions. However, a counterexample is given by Collis & Lele (1999), where receptivity to roughness close to the leading edge of a parabolic body is investigated through DNS. The results show that receptivity is enhanced by convex surface curvature and suppressed by non-parallelism—effects that are not captured by FRNT. Comparing the receptivity coefficients from DNS with those from theoretical approaches, these authors conclude that the prediction of crossflow instability receptivity near a leading edge must account for the strongly non-parallel flow around the upstream neutral point. Unfortunately, stability predictions using a perturbation approach for non-parallel effects proved inadequate for the most dangerous crossflow mode at the conditions studied in that work. A similar indication for the relevance of the leading-edge region is seen in the results by Schrader *et al.* (2009) when analysing receptivity to free-stream vortical modes.

To conclude, the good news is that receptivity coefficients obtained for single modes appear to be sufficient in order to predict the disturbance behaviour in swept boundary layers even in the presence of free-stream turbulence of moderate amplitude. On the other hand, simple perturbation approaches for theoretical non-parallel receptivity prediction may prove inadequate. More research is, in fact, needed to verify this claim.

The authors wish to acknowledge Philipp Schlatter, Antonios Monokrousos, Ardeshir Hanifi, Henrik Alfredsson and Dan Henningson for fruitful discussions. The PSE data used were kindly provided by David Tempelmann. This research is supported by VR (The Swedish Research Council). Computer time provided by SNIC (Swedish National Infrastructure for Computing) at the Center for Parallel Computers (PDC), KTH, and at the National Supercomputer Centre, Linköpings universitet, is gratefully acknowledged.

REFERENCES

Bippes, H. 1999 Basic experiments on transition in three-dimensional boundary layers dominated by crossflow instability. *Prog. Aerosp. Sci.* **35**, 363–412.

Bonfigli, G. 2006 Numerical simulation of transition and early turbulence in a 3-d boundary layer perturbed by superposed stationary and travelling crossflow vortices. PhD thesis, Universität Stuttgart.

Bonfigli, G. & Kloker, M. 2007 Secondary instability of crossflow vortices: validation of the stability theory by direct numerical simulation. *J. Fluid Mech.* **583**, 229–272.

Brandt, L. & de Lange, H. C. 2008 Streak interactions and breakdown in boundary layer flows. *Phys. Fluids* **20** (024107), 1–16.

Brandt, L., Schlatter, P. & Henningson, D. S. 2004 Transition in boundary layers subject to free-stream turbulence. *J. Fluid Mech.* **517**, 167–198.

Chevalier, M., Schlatter, P., Lundbladh, A. & Henningson, D. S. 2007 A pseudo-spectral solver for incompressible boundary layer flows. *Tech. Rep.* TRITA-MEK 2007:07. Royal Institute of Technology (KTH), Dept. of Mechanics, Stockholm.

Choudhari, M. 1994 Roughness-induced generation of crossflow vortices in three-dimensional boundary layers. *Theoret. Comput. Fluid Dyn.* **6**, 1–30.

Collis, S. S. & Lele, S. K. 1999 Receptivity to surface roughness near a swept leading edge. *J. Fluid Mech.* **380**, 141–168.

Crouch, J. D. 1992 Localized receptivity of boundary layers. *Phys. Fluids* A **4** (7), 1408–1414.

Crouch, J. D. 1993 Receptivity of three-dimensional boundary layers. *AIAA Paper* 93-0074.

Deyhle, H. & Bippes, H. 1996 Disturbance growth in an unstable three-dimensional boundary layer and its dependence on environmental conditions. *J. Fluid Mech.* **316**, 73–113.

Fransson, J. H. M., Matsubara, M. & Alfredsson, P. H. 2005 Transition induced by free-stream turbulence. *J. Fluid Mech.* **527**, 1–25.

Haynes, T. S. & Reed, H. L. 2000 Simulation of swept-wing vortices using nonlinear parabolized stability equations. *J. Fluid Mech.* **405**, 325–349.

Herbert, T. 1988 Secondary instability of boundary layers. *Annu. Rev. Fluid Mech.* **20**, 487–526.

Hœpffner, J. & Brandt, L. 2008 Stochastic approach to the receptivity problem applied to bypass transition in boundary layers. *Phys. Fluids* **20** (024108), 1–4.

Högberg, M. & Henningson, D. S. 1998 Secondary instability of crossflow vortices in Falkner–Skan–Cooke boundary layers. *J. Fluid Mech.* **368**, 339–357.

Jacobs, R. G. & Durbin, P. A. 1998 Shear sheltering and continuous spectrum of the Orr–Sommerfeld equation. *Phys. Fluids* **10** (8), 2006–2011.

Jacobs, R. G. & Durbin, P. A. 2001 Simulations of bypass transition. *J. Fluid Mech.* **428**, 185–212.

Jeong, J. & Hussain, F. 1995 On the identification of a vortex. *J. Fluid Mech.* **285**, 69–94.

Kachanov, Y. S. 1994 Physical mechanisms of laminar boundary-layer transition. *Annu. Rev. Fluid Mech.* **26**, 411–482.

Klebanoff, P. S. 1971 Effect of free-stream turbulence on the laminar boundary layer. *Bull. Am. Phys. Soc.* **10**, 1323.

Malik, M. R., Li, F., Choudhari, M. M. & Chang, C.-L. 1999 Secondary instability of crossflow vortices and swept-wing boundary-layer transition. *J. Fluid Mech.* **399**, 85–115.

Malik, M. R., Zang, T. A. & Hussaini, M. Y. 1985 A spectral collocation method for the Navier--Stokes equations. *J. Comp. Phys.* **61**, 64–88.

Matsubara, M. & Alfredsson, P. H. 2001 Disturbance growth in boundary layers subjected to free-stream turbulence. *J. Fluid Mech.* **430**, 149–168.

Monokrousos, A., Brandt, L., Schlatter, P. & Henningson, D. S. 2008 DNS and LES of estimation and control of transition in boundary layers subject to free-stream turbulence. *Intl J. Heat Fluid Flow* **29**, 841–855.

Nordström, J., Nordin, N. & Henningson, D. S. 1999 The fringe region technique and the Fourier method used in the direct numerical simulation of spatially evolving viscous flows. *SIAM J. Sci. Comp.* **20**, 1365–1393.

Poll, D. I. A. 1984 Transition description and prediction in three-dimensional flows. *Tech. Rep.* AGARD Rep. 709. Von Kármán Inst., Rhode-St-Genese, Belgium.

Pope, S. B. 2001 *Turbulent Flows*. Cambridge University Press.

Reibert, M. S., Saric, W. S., Carillo, R. B. & Chapman, K. L. 1996 Experiments in nonlinear saturation of stationary crossflow vortices in a swept-wing boundary layer. *AIAA Paper* 96-0184.

Saric, W. S., Jr., Carillo, R. B. & Reibert, M. S. 1998 Leading-edge roughness as a transition control mechanism. *AIAA Paper* 98-0781.

Saric, W. S., Reed, H. L. & White, E. B. 2003 Stability and transition of three-dimensional boundary layers. *Annu. Rev. Fluid Mech.* **35**, 413–440.

Schlatter, P. & Brandt, L. 2010 DNS of spatially-developing three-dimensional turbulent boundary layers. In *Direct and Large Eddy Simulation VII* (ed. V. Armenio, B. J. Guerts & J. Fröhlich) (in press).

Schlatter, P., de Lange, H. C. & Brandt, L. 2007 Numerical study of the stabilization of Tollmien–Schlichting waves by finite amplitude streaks. In *Turbulence and Shear Flow Phenomena 5* (ed. R. Friedrich, N. A. Adams, J. K. Eaton, J. A. C. Humphrey, N. Kasagi & M. A. Leschziner), vol. II, pp. 849–854.

Schlatter, P., Stolz, S. & Kleiser, L. 2004 LES of transitional flows using the approximate deconvolution model. *Intl J. Heat Fluid Flow* **25** (3), 549–558.

Schlatter, P., Stolz, S. & Kleiser, L. 2006 LES of spatial transition in plane channel flow. *J. Turbul.* **7** (33), 1–24.

Schmid, P. J. & Henningson, D. S. 2001 *Stability and Transition in Shear Flows*. Springer.

Schrader, L.-U., Brandt, L. & Henningson, D. S. 2009 Receptivity mechanisms in three-dimensional boundary-layer flows. *J. Fluid Mech.* **618**, 209–241.

Stolz, S., Adams, N. A. & Kleiser, L. 2001 An approximate deconvolution model for large-eddy simulation with application to incompressible wall-bounded flows. *Phys. Fluids* **13** (4), 997–1015.

Taylor, G. I. 1939 Some recent developments in the study of turbulence. In *Proceedings of the Fifth International Congress for Applied Mechanics* (ed. J. P. Den Hartog & H. Peters), pp. 294–310. Wiley.

Tempelmann, D., Hanifi, A. & Henningson, D. S. 2010 Spatial optimal growth in three-dimensional boundary layers. *J. Fluid Mech.* **646**, pp. 5–37.

Tufo, H. M. & Fischer, P. F. 1999 Terascale spectral element algorithms and implementations. In *Supercomputing, ACM/IEEE 1999 Conference*. Portland, USA.

Wassermann, P. & Kloker, M. 2002 Mechanisms and passive control of crossflow-vortex-induced transition in a three-dimensional boundary layer. *J. Fluid Mech.* **456**, 49–84.

Wassermann, P. & Kloker, M. 2003 Transition mechanisms induced by travelling crossflow vortices in a three-dimensional boundary layer. *J. Fluid Mech.* **483**, 67–89.

Westin, K. J. A., Boiko, A. V., Klingmann, B. G. B., Kozlov, V. V. & Alfredsson, P. H. 1994 Experiments in a boundary layer subjected to free stream turbulence. Part 1. Boundary layer structure and receptivity. *J. Fluid Mech.* **281**, 193–218.

White, E. B. & Saric, W. S. 2005 Secondary instability of crossflow vortices. *J. Fluid Mech.* **525**, 275–308.

White, E. B., Saric, W. S., Gladden, R. D. & Gabet, P. M. 2001 Stages of swept-wing transition. *AIAA Paper* 2001-0271.

Wintergerste, T. & Kleiser, L. 1997 Breakdown of a crossflow vortex in a three-dimensional boundary layer. In *Direct and Large Eddy Simulation II* (ed. J.-P. Chollet), pp. 179–190. Kluwer.

Zaki, T. A. & Durbin, P. A. 2005 Mode interaction and the bypass route to transition. *J. Fluid Mech.* **531**, 85–111.

Zaki, T. A. & Saha, S. 2009 On shear sheltering and the structure of vortical modes in single- and two-fluid boundary layers. *J. Fluid Mech.* **626**, 111–147.